TECHNICAL RESEARCH REPORT

Wavelet-based Multiresolution Local Tomography

by F. Rashid-Farrokhi, K.J.R. Liu,
C.A. Berenstein, and D. Walnut

T.R. 95-73

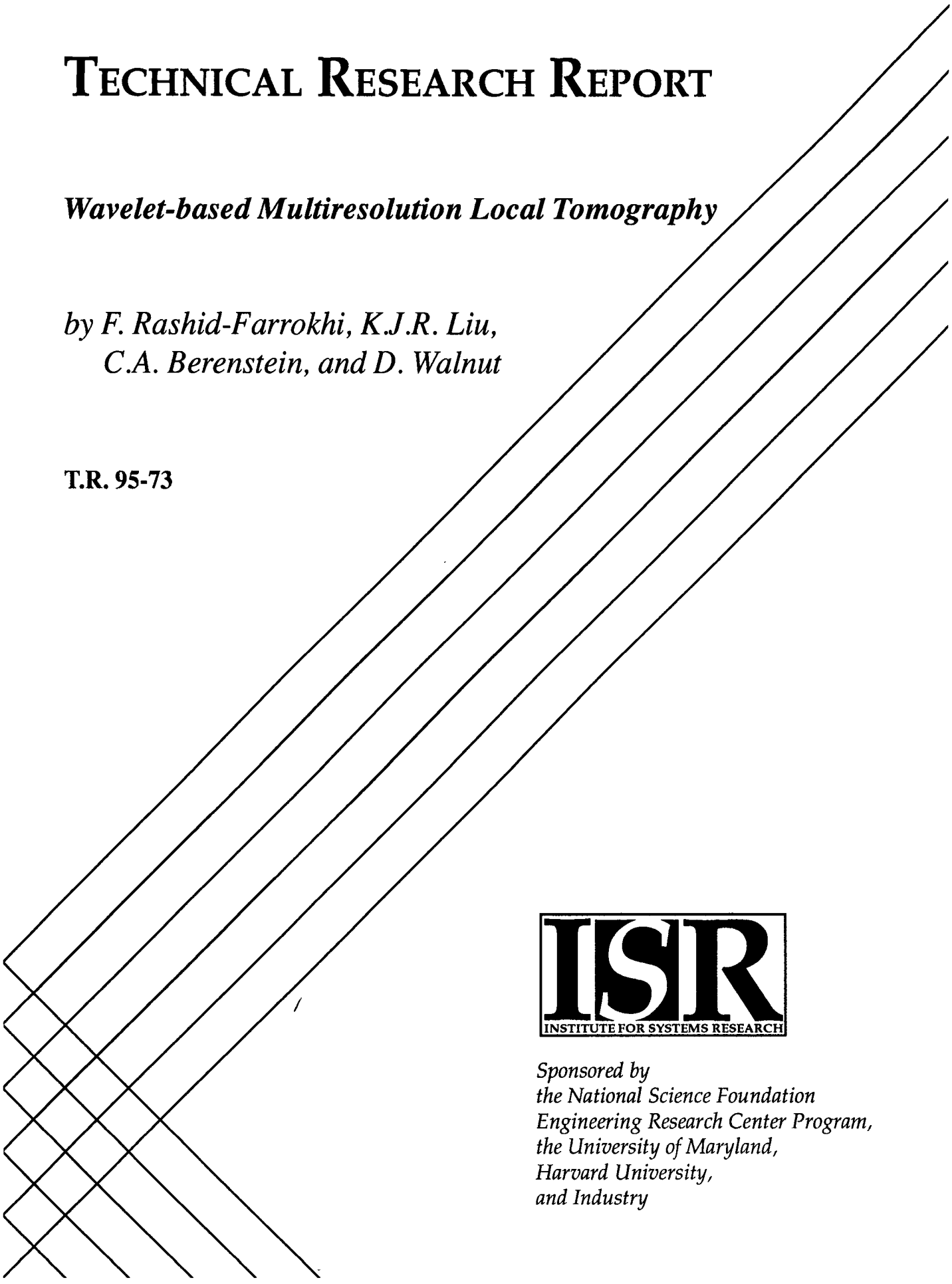

Sponsored by
the National Science Foundation
Engineering Research Center Program,
the University of Maryland,
Harvard University,
and Industry

Wavelet-based Multiresolution Local Tomography

F. Rashid-Farrokhi, K. J. R. Liu, C. A. Berenstein[1], and D. Walnut[2]

Electrical Engineering Department and Institute for Systems Research
University of Maryland
College Park, MD 20742, USA

[1] Department of Mathematical Sciences and Institute for System Research
University of Maryland
College Park, MD 20742, USA

[2] Department of Mathematical Sciences
George Mason University
Fairfax, VA, 22030, USA

ABSTRACT

We develop an algorithm to reconstruct the wavelet coefficients of an image from the Radon transform data. The proposed method uses the properties of wavelets to localize the Radon transform and can be used to reconstruct a local region of the cross section of a body, using almost completely local data which significantly reduces the amount of exposure and computations in X-ray tomography. This property which distinguishes our algorithm from the previous algorithms is based on the observation that for some wavelet basis with sufficiently many vanishing moments, the ramp-filtered version of the scaling function as well as the wavelet function has extremely rapid decay. We show that the variance of the elements of the null-space is negligible in the locally reconstructed image. Also we find an upper bound for the reconstruction error in terms of the amount of data used in the algorithm. To reconstruct a local region 20 pixels in radius in a 256×256 image we require 12.5% of full exposure data while the previous methods can reduce the amount of exposure only to 40% for the same case.

Keywords: Local Tomography, Wavelet, Multiresolution.

This work is supported in part by the NSF grant MIP9457397.

I. Introduction

It is well known that in dimension two and in fact in any even dimension the Radon transform is not local, that is, the recovery of an image at any fixed point requires the knowledge of all projections of the image. This means that a patient would have to be exposed to a relatively large amount of X-rays even if it was desired to view only a small part of the patient's body. Thus, searching for a means to reduce exposure, and at the same time to be able to perfectly reconstruct the region of interest, has been of great interest recently [3], [4], [8], [9].

The use of wavelets to localize the Radon transform was first proposed in [1]. This paper proposed the principle that the Hilbert transform of a function with many vanishing moments should decay very rapidly. This is related to the notion that certain singular integral operators are almost diagonalized by wavelets [12]. It was proposed in [1], that high frequency features of an image can be recovered locally using the wavelet transform. In [8], Olson and DeStefano reconstruct the local values of f from the one dimensional wavelet transform of $R_\theta f$. In [9], Delaney and Bresler compute the two dimensional separable wavelet transform of the image directly from the projection data. Both algorithms in [8] and [9] take advantage of the observation, made in [1], that the Hilbert transform of a function with many vanishing moments has rapid decay. In fact, the Hilbert transform of a compactly supported wavelet with sufficiently many vanishing moments has essentially the same support as the wavelet itself. Thus, in both algorithms, the high-resolution parts of the image are obtained locally, and the low-resolution parts are obtained by global measurements of the full exposure projections at a few angles.

We have made the surprising observation that, in some cases, the Hilbert transform of a compactly supported *scaling function* also has essentially the same support as the scaling function itself. This phenomena is related to the number of vanishing moments of the scaling function of an orthonormal or biorthonormal wavelet basis. That is, if $\phi(t)$ is such a scaling function, and if $\hat{\phi}^{(j)}(0) = 0$ for $j = 1, 2, \ldots, K$, for some large K, then the Hilbert transform of ϕ will have rapid decay. We take advantage of this observation to reconstruct the low-resolution parts of the image as well as the high-resolution parts using almost local data plus a small margin for the support of the filters. This gives substantial savings in exposure and computation over the methods in [8] and [9]. For example in order to reconstruct a local region 20 pixels in radius in a 256×256 image we require 12.5% of

full exposure data while the proposed methods in [8], [9] can reduce the amount of exposure only to 40% for the same case.

The algorithms in [8], [9] are not strictly local tomography algorithms, since they use measurements far from the region of interest at a sparse set of angles. Our algorithm is close to a true local tomography algorithm, since we use only essentially local measurements to reconstruct the local values of f. It can be compared with the technique of Λ-Tomography, which is used to reconstruct the function $\Lambda f - \mu\Lambda^{-1} f$ rather than the density function f. This reconstruction gives an edge representation of the original image. Recently it has been shown that the magnitude of jump discontinuities in an image can be recovered using this technique [3], [4].

It has been noted in a number of places [14], [15], [16], that the recovery of a function f in a local region from only its projections on lines intersecting that region is not uniquely solvable. In other words, the interior Radon transform has a non-trivial null-space. It has been observed that there exist functions which are non-zero in a local region, but whose projections are zero on lines passing through that region (Fig. 7). It has been shown that the elements of the null-space of the interior Radon transform do not vary much in the region of interest [14]. In our algorithm this phenomenon appears as a constant bias in the reconstructed image. Such a bias is commonly observed in the local reconstruction problem [14], [16].

In this paper we will present an algorithm to reconstruct the wavelet and scaling coefficients of an image directly from its projections. This is useful in applications where the wavelet coefficients of the reconstructed image are used; in that it saves the computations required to obtain the wavelet coefficients from the reconstructed image. We also show how this reconstruction technique leads to a local tomography algorithm which uses the projections of the image on lines intersecting the local region of interest plus a small number of projections, in the immediate vicinity, to obtain a very good approximation of the image in the region of interest.

The main features of our algorithm are:

- Reduced exposure compared to previous algorithms (cf. [9], [8]). In our algorithm there is no need to obtain a rough estimate of the global properties of the Radon transform by sparsely sampled full exposure projections. We just compute a small number of projections on lines passing close to the region of interest to reconstruct the local values of the image up to a constant bias.

- Computationally more efficient than other algorithms, because it uses fewer projections overall to locally reconstruct the image.
- Uniform exposure at all angles which allows for easier implementation in hardware. (In the algorithms proposed in [8] and [9], different amount of projections have to be computed with variable lengths for different angles.)
- Ability to reconstruct off-center or even multiple regions of interest, as well as centered reconstruction.
- Applicable to the cases where the wavelet basis is not separable and there exists no multiresolution approach to obtain the wavelet coefficients. (The method proposed in [9] can only be used for separable wavelet bases.)
- Reconstruction of the wavelet coefficients of the image with the same complexity as the conventional filtered backprojection method.

This paper is organized as follows: In section II we will briefly introduce the Radon transform, discuss the non-locality of the Radon transform and the conventional reconstruction technique, i.e., the filtered backprojection method. In section III after reviewing the basics of the wavelet transform, we will introduce a full-data reconstruction technique based on the wavelet transform. We will discuss the locality property of the proposed algorithm in section IV. Section V then discusses the implementation of this method and in section VI the simulation results will be presented.

II. Preliminaries and notations

In this section, we will briefly introduce the terminology and definitions required in the subsequent discussions. In this paper we use the following notations: The d dimensional Euclidean space is denoted by R^d. Given a set $S \subset R^d$, $\mathbf{1}_S$ denotes the indicator function of S. We define the Fourier transform in R^d by $\hat{f}(\vec{\omega}) = \int_{R^d} f(\vec{x}) e^{j2\pi\vec{\omega}\cdot\vec{x}} d\vec{x}$. The inverse Fourier transform is defined by $\mathcal{F}^{-1}(\hat{f}(\vec{\omega}))(\vec{x}) = \int_{R^d} \hat{f}(\vec{\omega}) e^{-j2\pi\vec{\omega}\cdot\vec{x}} d\vec{w}$. The space of infinitely differentiable functions, all of whose derivatives decay faster than any polynomial is denoted as $S(R^d)$. Both continuous and discrete convolution operators are denoted by $*$.

A. Radon transform

In Computerized Tomography (CT), a cross section of the human body is scanned by a non-diffracting thin X-ray beam whose intensity loss is recorded by a set of detectors. The Radon Transform (RT) is a mathematical tool which is used to describe the recorded intensity losses as averages of the tissue density function over hyper-planes which, in dimension two, are lines. Given $f \in S(R^2)$, restricted to a disc of radius one, we define the Radon transform of f by

$$R_\theta f(s) \;=\; \int_{\vec{x}\cdot\vec{\theta}=s} f(\vec{x})d\vec{x} \;=\; \int_{\theta^\perp} f(s\vec{\theta}+y)dy, \tag{1}$$

where $\vec{\theta} = (\cos\theta, \sin\theta), \theta \in [0, 2\pi)$, $s \in R$ and $\theta^\perp$ is the subspace perpendicular to $\vec{\theta}$.

The interior Radon transform [15] [16] is the Radon transform restricted to lines passing through the region of interest (ROI) which is a circle of radius r ($r < 1$) about the origin. It is defined by

$$R_\theta f(s) \;\rightarrow\; R_\theta f(s)\; \mathbf{1}_{[-r,r]}(s). \tag{2}$$

The problem of recovery of f from the interior Radon transform is called the *interior problem* or *region of interest tomography.* The interior problem in dimension two is not uniquely solvable, i.e., there are functions which are not zero in the region of interest but whose projections on lines intersecting that region are zero. However, these functions do not vary much inside the region of interest, and in fact a crude approximation to the missing projections suffices to approximate f well inside the region of interest up to an additive constant [14].

B. Reconstruction

The basic formula for inverting the Radon transform is based on the fact that the Fourier transform of the Radon transform with respect to the variable s is the Fourier transform of the function f along a line passing through the origin. This property is known as the projection theorem or Fourier slice theorem:

$$(\widehat{R_\theta f})(\omega) = \hat{f}(\omega\vec{\theta}), \quad \omega \in R. \tag{3}$$

Thus the Fourier transform of the projections at enough angles could in principle be assembled into a complete description of the two dimensional Fourier transform of the image and then simply inverted to arrive at the function f. Using the polar Fourier inversion formula and the Fourier slice

theorem, we can reconstruct the function f from the projection data $R_\theta f(s)$ by

$$f(\vec{x}) = \int_0^\pi \int_{-\infty}^\infty (\widehat{R_\theta f})(\omega) e^{j2\pi\omega(\vec{x}\cdot\vec{\theta})} |\omega| d\omega d\theta. \tag{4}$$

The above formula, called the filtered backprojection formula, can be implemented in two steps, the filtering step, which in the Fourier domain can be written as

$$\widehat{Q}_\theta(\omega) = \widehat{R_\theta f}(\omega)|\omega|, \tag{5}$$

and the backprojection step,

$$f(\vec{x}) = \int_0^\pi Q_\theta(\vec{x}\cdot\vec{\theta}) d\theta. \tag{6}$$

Because $|\omega|$ is not bounded and filtering by this filter tends to magnify the high frequency noise, it is expedient in practice to multiply this operator by a smoothing window $W(\omega)$ as

$$\widehat{Q}_\theta(\omega) = \widehat{R_\theta f}(\omega)|\omega| W(\omega). \tag{7}$$

Therefore the reconstruction will result in an approximation of f rather than f itself. Normally the approximation has the form $e * f$, where e is an approximate delta function, called the point spread function [10]. The point spread function e is related to $W(\omega)$ by

$$W(\omega) = \hat{e}(\omega\cos\theta, \omega\sin\theta). \tag{8}$$

C. Non-locality of RT inversion

In (5) the Radon transform data is filtered by $|\omega|$. This operation can be formulated in the space domain as

$$Q_\theta(t) = H\ \partial\ R_\theta f(t), \tag{9}$$

where H is the Hilbert transform on R, and ∂ is ordinary differentiation. In the above equation the derivative part is a local operator, but the Hilbert transform

$$(\widehat{Hg})(\omega) = \frac{1}{i}\ sign(\omega)\hat{g}(\omega) \tag{10}$$

introduces a discontinuity in the derivative of the Fourier transform of a function at the origin. Hence the Hilbert transform of a compactly supported function can never be compactly supported.

This means that RT inversion based on (4) can not be accomplished locally, that is, in order to recover f exactly at a point $\vec{x}$, all projections of f are required and not just those on lines passing near $\vec{x}$. It has been noted that the above mentioned filtering will not increase the essential support of a function if the function's Fourier transform vanishes to high order at the origin [1], [8]. Wavelets which are in general constructed with as many zero moments as possible are good candidates for these functions.

III. Wavelet Reconstruction

A. Continuous Wavelet Transform

The wavelet transform has been an increasingly popular tool for signal and image processing. The transform decomposes the signal onto shifts and dilates of a function called the mother wavelet. In two dimensions, the wavelet transform is defined as follows. Let $g(\vec{t})$, $\vec{t} \in R^2$ satisfy

$$0 < \inf_{\theta\in[0,2\pi)} \int_0^\infty r^{-1}|\hat{g}(r\cos\theta, r\sin\theta)|^2 dr < \sup_{\theta\in[0,2\pi)} \int_0^\infty r^{-1}|\hat{g}(r\cos\theta, r\sin\theta)|^2 dr < \infty. \tag{11}$$

Let $\tilde{g}(\vec{t}) = g(-\vec{t}), \vec{t} \in R^2$, and define the continuous wavelet transform of f, on R^2, by

$$W_u^{(2)}(g; f)(\vec{v}) = \int_{R^2} f(\vec{t}) u g(u\vec{t} - \vec{v}) d\vec{t} = f * \tilde{g}_u(u^{-1}\vec{v}), \tag{12}$$

where $u \in R\backslash\{0\}$ and $\vec{v} = [x\ y] \in R^2$, and $g_u(\vec{v}) = ug(u\vec{v})$. In order to reconstruct the function f from its wavelet transform, we use

$$f(\vec{t}) = \int_{R^2} \int_R u^4 W_u^{(2)}(g; f)(\vec{v}) u g(u\vec{t} - \vec{v}) du d\vec{v}. \tag{13}$$

B. Multi-Resolution Wavelet Representation

In practice one prefers to write f as a discrete superposition of wavelets, therefore we define the discrete wavelet transform by

$$W_{2^j}^{(2)}(g; f)(\vec{n}) = \int_{R^2} f(\vec{t}) g_{2^j}(\vec{t} - 2^{-j}\vec{n}) d\vec{t}, \tag{14}$$

which is derived from (12) by setting $u = 2^j$ and $\vec{v} = \vec{n}$, where $j \in Z$ and $\vec{n} \in Z^2$.

Below we describe a multiresolution analysis approach to recovering $f(\vec{x})$ from its discrete wavelet transform (precise definitions and further details can be found in [7]). Let A_{2^j} be the operator which

approximates a measurable function $f(x)$ with finite energy ($f(x) \in L^2(R)$) at resolution 2^j. We consider the vector space $V_{2^j} \subset L^2(R)$ as the set of all possible approximations at the resolution of 2^j of functions in $L^2(R)$, such that $\forall j \in Z$, $V_{2^j} \subset V_{2^{j+1}}$. For each multiresolution approximation V_{2^j}, there exists a unique function $\phi(x) \in L^2(R)$, called a scaling function such that $\{\phi_{2^j}(x - 2^{-j}n)\}_{n \in Z}$ is an orthonormal basis of V_{2^j}, where $\phi_{2^j}(x) = 2^{j/2}\phi(2^j x)$. Therefore the projection on V_{2^j} can be computed by decomposing the function $f(x)$ on this basis, i.e.,

$$A_{2^j} f(x) = \sum_{n=-\infty}^{\infty} \langle f(u), \phi_{2^j}(u - 2^{-j}n)\rangle \phi_{2^j}(x - 2^{-j}n). \tag{15}$$

The coefficients in the above sum are the discrete approximation of $f(x)$ at the resolution 2^j, defined by

$$\begin{aligned} A^d_{2^j} f(n) &= \langle f(u), \phi_{2^j}(u - 2^{-j}n)\rangle \\ &= \int f(u)\phi_{2^j}(u - 2^{-j}n)du = (f(u) * \tilde{\phi}_{2^j}(u))(2^{-j}n), \end{aligned} \tag{16}$$

where $\tilde{\phi}_{2^j}(x) = \phi_{2^j}(-x)$.

In practice, we assume that the given discrete function $f(n)$ is the approximation of $f(x)$ at resolution 1. In a multiresolution approximation the discrete approximation at resolution 2^j can be found from the discrete approximation at resolution 2^{j+1} by

$$A^d_{2^j} f(n) = \sum_{k=-\infty}^{\infty} h(k - 2n) A^d_{2^{j+1}} f(k), \tag{17}$$

where $h(n) = \langle \phi_{2^{-1}}(u), \phi(u - n)\rangle$. The Fourier transform of $h(n)$, denoted by $H(\omega)$, is defined as

$$H(\omega) = \sum_{n=-\infty}^{\infty} h(n) e^{-jn\omega}. \tag{18}$$

The Fourier transform of $\phi(x)$ is given by

$$\hat{\phi}(\omega) = \prod_{p=1}^{\infty} H(2^p \omega), \tag{19}$$

and

$$\hat{\phi}_{2^j}(\omega) = \hat{\phi}(\omega) \prod_{p=1}^{j} H(2^{p-1}\omega). \tag{20}$$

The difference in information between the approximation of function $f(x)$ at resolution 2^{j+1} and 2^j, called the detail signal at the resolution 2^j, corresponds to the projection of f on the orthogonal

complement of V_{2^j} in $V_{2^{j+1}}$, denoted by O_{2^j}. Define the function $\psi(x)$, the mother wavelet, by $\hat{\psi}(\omega) = G(\omega/2)\hat{\phi}(\omega/2)$, where $G(\omega) = e^{-j\omega}\overline{H(\omega+\pi)}$. The set of functions $\{2^{-j/2}\psi_{2^j}(x-2^{-j}n)\}_{n\in Z}$ is an orthonormal basis of O_{2^j}. It can be easily shown that

$$\hat{\psi}_{2^j}(\omega) = \begin{cases} \hat{\phi}(\omega)G(2^{j-1}\omega)\prod_{p=1}^{j-1}H(2^{p-1}\omega) & \text{if } j>1 \\ \hat{\phi}(\omega)G(\omega) & \text{if } j=1 \end{cases}. \tag{21}$$

The projection of $f(x)$ on the vector space O_{2^j} is given by

$$D_{2^j}f(x) = \sum_{n=-\infty}^{\infty}\langle f(u),\psi_{2^j}(u-2^{-j}n)\rangle\psi_{2^j}(x-2^{-j}n). \tag{22}$$

The coefficients in the above formula, called the detail coefficients, are defined as

$$D^d_{2^j}f(n) = \langle f(u),\psi_{2^j}(u-2^{-j}n)\rangle = (f(u)*\tilde{\psi}_{2^j}(u))(2^{-j}n), \tag{23}$$

that is, the difference of information between $A^d_{2^{j+1}}f(n)$ and $A^d_{2^j}f(n)$. The detail coefficients at resolution 2^j can be obtained from the approximation at resolution 2^{j+1} by

$$D^d_{2^j}f(n) = \sum_{k=-\infty}^{\infty} g(k-2n)A^d_{2^{j+1}}f(k), \tag{24}$$

where $g(n) = \langle\psi_{2^{-1}}(u),\phi(u-n))\rangle$. The impulse response of the filter $g(n)$ is related to the filter $h(n)$ by

$$g(n) = (-1)^{1-n}\,h(1-n). \tag{25}$$

Finally, for any $J>0$, the original discrete signal $A^d_1f(n)$, measured at resolution 1, can be represented by $(A^d_{2^J}f, D^d_{2^j}f)_{-J\le j\le -1}$, which is called the orthogonal wavelet representation of the signal. The approximation at resolution 2^{j+1} can be obtained by combining the detail and approximation at resolution 2^j, i.e.,

$$A^d_{2^{j+1}}f(n) = 2\sum_{k=-\infty}^{\infty}h(n-2k)A^d_{2^j}f(k) + 2\sum_{k=-\infty}^{\infty}g(n-2k)D^d_{2^j}f(k). \tag{26}$$

This formula can be used in a pyramidal structure to reconstruct A^d_1f, the approximation at resolution 1, from the set $(A^d_{2^J}f, D^d_{2^j}f)_{-J\le j\le -1}$.

Similar to 1-D functions, we can construct a multiresolution approximation in $L^2(R^2)$. Letting $\Phi(x,y) = \phi(x)\phi(y)$, where ϕ is the scaling function for a 1-D multiresolution approximation, it can be shown that

$$\{\Phi_{2^j}(x-2^{-j}n, y-2^{-j}m)\}_{(n,m)\in Z^2} \tag{27}$$

forms an orthonormal basis for V_{2^j}, in a multiresolution approximation in $L^2(R^2)$, where $\Phi_{2^j}(x,y) = \Phi(2^j x, 2^j y) = \phi_{2^j}(x)\phi_{2^j}(y)$. The projection onto V_{2^j} can therefore be computed in this case by

$$A_{2^j} f(x,y) = \sum_{n=-\infty}^{\infty} \sum_{m=-\infty}^{\infty} \langle f(u,v), \phi_{2^j}(u - 2^{-j}n)\phi_{2^j}(v - 2^{-j}m)\rangle \phi_{2^j}(x - 2^{-j}n)\phi_{2^j}(y - 2^{-j}m). \quad (28)$$

The discrete approximation at resolution 2^j is defined by

$$A^d_{2^j} f(n,m) = (f(u,v) * \tilde{\phi}_{2^j}(u)\tilde{\phi}_{2^j}(v))(2^{-j}n, 2^{-j}m). \quad (29)$$

The difference between the approximation $A_{2^j} f(x,y)$ and $A_{2^{j+1}} f(x,y)$, called the detail signal at resolution 2^j, corresponds to the projection of f on the orthogonal complement of V_{2^j} in $V_{2^{j+1}}$, denoted by O_{2^j}. Let $\Psi^1(x,y) = \phi(x)\psi(y)$, $\Psi^2(x,y) = \psi(x)\phi(y)$ and $\Psi^3(x,y) = \psi(x)\psi(y)$, then the set of functions

$$\{\Psi^1_{2^j}(x - 2^{-j}n, y - 2^{-j}m), \Psi^2_{2^j}(x - 2^{-j}n, y - 2^{-j}m), \Psi^3_{2^j}(x - 2^{-j}n, y - 2^{-j}m)\}_{(n,m)\in Z^2}, \quad (30)$$

where $\Psi^i_{2^j}(x,y) = 2^j \Psi^i(2^j x, 2^j y)$, is an orthonormal basis for O_{2^j}. The projection of $f(x,y)$ on the vector space O_{2^j} is given by

$$\begin{aligned}
D^d_{2^j,1} f(x,y) &= \sum_{n=-\infty}^{\infty} \sum_{m=-\infty}^{\infty} \langle f(u,v), \phi_{2^j}(u - 2^{-j}n)\psi_{2^j}(v - 2^{-j}m)\rangle \phi_{2^j}(x - 2^{-j}n)\psi_{2^j}(y - 2^{-j}m) \\
D^d_{2^j,2} f(x,y) &= \sum_{n=-\infty}^{\infty} \sum_{m=-\infty}^{\infty} \langle f(u,v), \psi_{2^j}(u - 2^{-j}n)\phi_{2^j}(v - 2^{-j}m)\rangle \psi_{2^j}(x - 2^{-j}n)\phi_{2^j}(y - 2^{-j}m) \\
D^d_{2^j,3} f(x,y) &= \sum_{n=-\infty}^{\infty} \sum_{m=-\infty}^{\infty} \langle f(u,v), \psi_{2^j}(u - 2^{-j}n)\psi_{2^j}(v - 2^{-j}m)\rangle \psi_{2^j}(x - 2^{-j}n)\psi_{2^j}(y - 2^{-j}m). \quad (31)
\end{aligned}$$

The detail coefficients are given by

$$\begin{aligned}
D^d_{2^j,1} f(n,m) &= (f(x,y) * 2^{-j}\tilde{\phi}_{2^j}(x)\tilde{\psi}_{2^j}(y))(2^{-j}n, 2^{-j}m) \\
D^d_{2^j,2} f(n,m) &= (f(x,y) * 2^{-j}\tilde{\psi}_{2^j}(x)\tilde{\phi}_{2^j}(y))(2^{-j}n, 2^{-j}m) \\
D^d_{2^j,3} f(n,m) &= (f(x,y) * 2^{-j}\tilde{\psi}_{2^j}(x)\tilde{\psi}_{2^j}(y))(2^{-j}n, 2^{-j}m), \quad (32)
\end{aligned}$$

where $(n,m) \in Z^2$. Fig. 1(a) shows the conventional filter bank which is usually used to obtain approximation and details of a signal.

The discrete approximation at resolution 2^{j+1} can be obtained by combining the detail and approximation at resolution 2^j, i.e.,

$$A^d_{2^{j+1}} f(n,m) = 2 \sum_{k=-\infty}^{\infty} \sum_{l=-\infty}^{\infty} h(n-2k)h(m-2l) A^d_{2^j} f(k,l)$$

$$+ \quad 2 \sum_{k=-\infty}^{\infty} \sum_{l=-\infty}^{\infty} h(n-2k)g(m-2l)D^d_{2^j,1}f(k,l)$$
$$+ \quad 2 \sum_{k=-\infty}^{\infty} \sum_{l=-\infty}^{\infty} g(n-2k)h(m-2l)D^d_{2^j,2}f(k,l)$$
$$+ \quad 2 \sum_{k=-\infty}^{\infty} \sum_{l=-\infty}^{\infty} g(n-2k)g(m-2l)D^d_{2^j,3}f(k,l). \tag{33}$$

Therefore in order to recover the approximation at level $j+1$, the approximations at level j are filtered by $h(m)h(n)$, and the detail coefficients are filtered by $h(n)g(m)$, $g(n)h(m)$, and $g(n)g(m)$ respectively. These wavelet reconstruction filters in the Fourier domain are given by

$$H_r^A(\omega_1,\omega_2) = H(\omega_1)H(\omega_2)$$
$$H_r^{D^1}(\omega_1,\omega_2) = H(\omega_1)G(\omega_2)$$
$$H_r^{D^2}(\omega_1,\omega_2) = G(\omega_1)H(\omega_2)$$
$$H_r^{D^3}(\omega_1,\omega_2) = G(\omega_1)G(\omega_2). \tag{34}$$

In those applications that we are interested in, namely recovering a local region of the image from the approximate and detail coefficients, we have to calculate these coefficients for that region plus a margin for the support of the wavelet reconstruction filters. That margin is equal to half of the length of the filters h and g. Fig. 1(b) shows the block diagram of the analysis filter bank which obtains the approximation at level j from the approximations and detail at level $j-1$. This block diagram can be used in a pyramidal structure to reconstruct $A^d_1 f$, the approximation at resolution 1, from the set $(A^d_{2^J} f, D^d_{2^j} f)_{-J \le j \le -1}$.

In order to have fast computation (and also to do effective local reconstruction), the filters must be short. On the other hand, it is desirable to have linear phase FIR filters which can be easily cascaded in a pyramidal structure. Unfortunately the only symmetric perfect reconstruction filters with linear phase are Haar filters [5], so we relax the orthonormality property and we use a biorthonormal basis. The only difference is that the synthesis filters h, g, are different from the analysis filters $\breve{h}$ and $\breve{g}$ and must satisfy

$$\breve{g}_n = (-1)^n h_{-n-1}, \quad g_n = (-1)^n \breve{h}_{-n-1}, \quad \sum_n h_n \breve{h}_{n+2k} = \delta_{k,0}. \tag{35}$$

C. Wavelet Reconstruction from the Projection Data

In this section we present an algorithm which can be used to obtain the wavelet coefficients of a function on R^2 from its Radon transform data. In those applications for which one is interested in the wavelet coefficients of the function, it involves fewer computations than first reconstructing the function and then taking its wavelet transform. Also using this method one can obtain locally the wavelet coefficients of a function, which will allow the local reconstruction of a function and can be used in local tomography. This property will be explained in section IV. We first introduce the main formulas for the reconstruction of the continuous wavelet transform directly from the Radon transform data.

Given a real-valued, square integrable function g on R^2 which satisfies condition (11), let f be given on R^2, the wavelet transform of function f can be reconstructed from its 1-D projections by

$$\begin{aligned} W_u^{(2)}(g;f)(\vec{v}) &= f * \tilde{g}_u(u\vec{v}) \\ &= u^{1/2}\int_0^{\pi}(H\partial R_\theta \tilde{g}_u * R_\theta f)((u^{-1}x)\cos\theta + (u^{-1}y)\sin\theta)d\theta, \end{aligned} \tag{36}$$

where $\vec{v} = [x\ y] \in R^2$. In the discrete case the above equation becomes:

$$W_{2^j}^{(2)}(g;f)(\vec{n}) = \int_0^{\pi}(H\partial R_\theta \tilde{g}_{2^j} * R_\theta f)((2^{-j}n_1)\cos\theta + (2^{-j}n_2)\sin\theta)d\theta, \tag{37}$$

where $\vec{n} = [n_1\ n_2]$. The right-hand-side can be evaluated in two steps, the filtering step,

$$Q_{2^j,\theta}(t) = (R_\theta f * H\partial R_\theta \tilde{g}_{2^j})(2^{-j}t), \tag{38}$$

and the backprojection step,

$$W_{2^j}^{(2)}(g;f)(\vec{n}) = \int_0^{\pi} Q_{2^j,\theta}(n_1\cos\theta + n_2\sin\theta)d\theta. \tag{39}$$

The filtering step can be implemented in Fourier domain as

$$\widehat{Q}_{2^j,\theta}(\omega) = \widehat{R_\theta f}(\omega)|\omega|\hat{\tilde{g}}_{2^j}(\omega\cos\theta, \omega\sin\theta)W(\omega), \tag{40}$$

where $\hat{\tilde{g}}_{2^j}(\omega_1,\omega_2)$, $\widehat{Q}_{2^j,\theta}(\omega)$ and $\widehat{R_\theta f}(\omega)$ are the Fourier transforms of the functions $\tilde{g}_{2^j}$, $Q_{2^j,\theta}$ and $R_\theta f$, respectively, and $W(\omega)$ is a smoothing window. Therefore (37) can be implemented using the same algorithm as the conventional filtered backprojection method while the ramp filter $|\omega|$ is replaced by the wavelet ramp filter $|\omega|\hat{\tilde{g}}_{2^j}(\omega\cos\theta, \omega\sin\theta)$.

If the wavelet basis is separable, the approximation and detail coefficients are given by (29) and (32). These coefficients can be obtained from the projection data by (37), replacing $g(\vec{v})$ by $\Phi(x,y) = \phi(x)\phi(x)$, $\Psi^1(x,y) = \phi(x)\psi(x)$, $\Psi^2(x,y) = \psi(x)\phi(x)$, and $\Psi^3(x,y) = \psi(x)\psi(x)$, respectively. For example, the approximation coefficients are obtained by

$$A^d_{2^j} f(n,m) = W^{(2)}_{2^j}(\Phi; f)([n\ m]) = 2^{j/2} \int_0^\pi (H\partial R_\theta \tilde{\Phi}_{2^j} * R_\theta f)((2^{-j}n)\cos\theta + (2^{-j}m)\sin\theta) d\theta. \quad (41)$$

These coefficients can be calculated using the standard filtered backprojection method, while the filtering part in the Fourier domain is given by

$$\hat{Q}_{A^d_{2^j},\theta}(\omega) = \hat{R}_\theta f(\omega) |\omega| \hat{\tilde{\Phi}}_{2^j}(\omega\cos\theta, \omega\sin\theta) W(\omega), \quad (42)$$

where $\hat{\tilde{\Phi}}_{2^j}(\omega\cos\theta, \omega\sin\theta) = \hat{\tilde{\phi}}_{2^j}(\omega\cos\theta)\hat{\tilde{\phi}}_{2^j}(\omega\sin\theta)$. The detail coefficients can be found in a similar way as

$$D^d_{2^j,i} f = W^{(2)}_{2^j}(\Psi^i; f)([n\ m]) \quad \text{for } i = 1,2,3. \quad (43)$$

To get the detail coefficients, the filtering step is modified as

$$\hat{Q}^i_{D_{2^j},\theta}(\omega) = \hat{R}_\theta f(\omega) |\omega| \hat{\tilde{\Psi}}^i_{2^j}(\omega\cos\theta, \omega\sin\theta) W(\omega) \quad \text{for } i = 1,2,3. \quad (44)$$

This means that the wavelet and scaling coefficients of the image can be obtained by filtered backprojection method while the ramp filter is replaced by

$$\begin{aligned}
H^A_\theta = |\omega| \hat{\tilde{\Phi}}^1_{2^j}(\omega\cos\theta, \omega\sin\theta) &= |\omega| \hat{\tilde{\phi}}_{2^j}(\omega\cos\theta) \hat{\tilde{\phi}}_{2^j}(\omega\sin\theta) \\
H^{D^1}_\theta = |\omega| \hat{\tilde{\Psi}}^1_{2^j}(\omega\cos\theta, \omega\sin\theta) &= |\omega| \hat{\tilde{\phi}}_{2^j}(\omega\cos\theta) \hat{\tilde{\psi}}_{2^j}(\omega\sin\theta) \\
H^{D^1}_\theta = |\omega| \hat{\tilde{\Psi}}^2_{2^j}(\omega\cos\theta, \omega\sin\theta) &= |\omega| \hat{\tilde{\psi}}_{2^j}(\omega\cos\theta) \hat{\tilde{\phi}}_{2^j}(\omega\sin\theta) \\
H^{D^1}_\theta = |\omega| \hat{\tilde{\Psi}}^3_{2^j}(\omega\cos\theta, \omega\sin\theta) &= |\omega| \hat{\tilde{\psi}}_{2^j}(\omega\cos\theta) \hat{\tilde{\psi}}_{2^j}(\omega\sin\theta), \quad (45)
\end{aligned}$$

which are called the scaling and wavelet ramp filters. In order to obtain pyramidal wavelet coefficients, the $A^d_{2^J} f$ and $D^d_{2^j,i} f$, $i = 1,2,3$, $-J \le j \le -1$ are found using (43) and (41). To reconstruct the image from these coefficients, we use the multiresolution reconstruction formulas (33). Fig. 2 shows the block diagram of the multiresolution reconstruction system. The reconstruction part uses the conventional multiresolution reconstruction filter bank (cf. Fig. 1), which appear as black boxes in the block diagram.

IV. Local Reconstruction

It has been noted [8] that if a function has a large number of vanishing moments (or, equivalently, if its Fourier transform vanishes to high order at the origin), then its Hilbert transform will decay very rapidly at infinity. If a compactly supported function has this property, then the essential support of its Hilbert transform should not be large. This phenomenon is in part a manifestation of the observation made in [12] that an integral operator with singular kernel of Calderon-Zygmund type is almost diagonalized in a wavelet basis.

More specifically, we can say that if a sufficiently smooth compactly supported function, f, has N vanishing moments, then $Hf(t) = O(|t|^{-N-1})$. To see why this is true, observe that if f has N vanishing moments, then $\widehat{Hf}$ has N continuous derivatives. That is, for any j, $\widehat{Hf}^{(j)}(\omega) = \hat{f}^{(j)}(\omega)$ if $\omega > 0$, and $-\hat{f}^{(j)}(\omega)$ if $\omega < 0$. Since $\hat{f}$ is analytic, $\hat{f}^{(j)}$ is continuous for all ω, and if $j \leq N$, then

$$\lim_{\omega \to 0+} \widehat{Hf}^{(j)}(\omega) = \lim_{\omega \to 0-} \widehat{Hf}^{(j)}(\omega) = 0.$$

Therefore, $\widehat{Hf}^{(j)}$ is continuous. If $j = N+1$, then $\widehat{Hf}^{(j)}$ is no longer continuous at $\omega = 0$ but is still bounded since

$$\lim_{\omega \to 0+} \widehat{Hf}^{(j)}(\omega) = \hat{f}^{(j)}(0), \quad \lim_{\omega \to 0-} \widehat{Hf}^{(j)}(\omega) = -\hat{f}^{(j)}(0).$$

Therefore, if f is sufficiently smooth that $\int \left|\hat{f}^{(j)}\right| < \infty$ for $j = 0, \ldots, N+1$, then

$$\sup_{t \in R} \left|t^{N+1} Hf(t)\right| \leq \frac{1}{2\pi^{N+1}} \int \left|\widehat{Hf}^{(N+1)}\right| \leq \frac{1}{2\pi^{N+1}} \int \left|\hat{f}^{(N+1)}\right| < \infty.$$

That is, for some number $C > 0$, depending on f,

$$|Hf(t)| \leq C(1 + |t|)^{-N-1}.$$

Therefore, if the function $R_\theta g(t)$ is compactly supported and has a large number of vanishing moments for each θ, then $H\partial R_\theta g$ should have very rapid decay. If g is a compactly supported wavelet basis function from (30) with sufficiently many vanishing moments, $H\partial R_\theta g$ has essentially the same support as $R_\theta g$ for each θ. The significance of this observation is that by (36) the discrete wavelet coefficients (43) can be computed locally using essentially local projections.

We have observed that even if g is replaced by scaling function given by (27), $H\partial R_\theta g$ has essentially the same support as $R_\theta g$ for each θ. Fig. 3 shows the Daubechies' biorthogonal wavelet and

scaling function (table III of [5]) as well as the ramp filtered version of these functions. Observe that the ramp-filtered scaling functions has almost the same essential support as the scaling function itself. [1] We have also observed that the angle dependent filters given by (45) have essentially the same support as the wavelet and scaling function for this wavelet basis. Therefore, in order to reconstruct the wavelet and scaling coefficients for some wavelet basis, we only need the projections passing through the region of interest plus a margin for the support of the wavelet and scaling ramp filters. Moreover, in order to reconstruct the image from the wavelet and scaling coefficients, we have to calculate these coefficients in the region of interest plus a margin for the support of the wavelet reconstruction filters (34). Since wavelet and scaling ramp filters and also the wavelet reconstruction filters get wider in lower scales, we need to increase the exposure to reconstruct the low resolution coefficients in the region of interest. In our algorithm we can reconstruct the scaling coefficients locally, henceforth we use only one level of wavelet filter bank. Thus we take full advantage of locality of wavelet and scaling function at high resolutions.

In order to quantify this locality phenomenon, we define the *spread* of a function f with respect to an interval I under ramp-filtering to be the normalized energy of the function $(|\omega|\hat{f}(\omega))\check{}(t)$ outside I, i.e., with $\overline{I}$ denoting the complement of I,

$$\int_{\overline{I}} |\mathcal{F}^{-1}(|\omega|\hat{f}(\omega))(t)|^2\, dt \;/\; \int_{-\infty}^{\infty} |\mathcal{F}^{-1}(|\omega|\hat{f}(\omega))(t)|^2\, dt.$$

The rapid decay of the ramp-filtered scaling functions is related to the number of vanishing moments of the scaling function. Orthonormal wavelets corresponding to scaling functions with vanishing moments have been called "coiflets" by Daubechies in [6, section 8.2]. For coiflets with 1, and 3 vanishing moments, supported on the intervals $[0, 5]$, and $[0, 11]$, respectively, we have measured spreads with respect to these intervals of .030 and .013 respectively. These scaling functions correspond to scaling filters with 6 and 12 taps respectively. Daubechies has also observed in [6, section 8.3.5] that the symmetric biorthogonal bases constructed in [5] are numerically very close to coiflets. For the biorthogonal "near-coiflet" scaling functions supported on the intervals $[0, 4]$, $[0, 8]$, and $[0, 12]$, we have measured spreads with respect to these intervals of .029, .016, and .0092 respectively. These scaling functions correspond to scaling filters with 5, 9, and 13 taps

[1] This is not the case in general, for example in Fig. 4 we have plotted another wavelet and scaling functions (table 6.2 of [6]) and their ramp-filtered versions, for comparison. The scaling function in this basis does spread significantly after ramp filtering.

respectively. For the purposes of this paper, it is most desirable to minimize both the spread of the scaling function and the number of taps in the corresponding filter. Under these criteria, the near-coiflet filter with 5 taps is near optimal (see Fig. 3(a) and (c), and Fig. 6(a)) and is therefore used in our simulations.

We assume that for each angle $\theta \in [0, 2\pi)$, the projection data $R_\theta f(s)$ is sampled with a radial sampling interval of T_s, and the support of f is a disk of radius R centered at the origin. The region of interest, a disc of radius r_i pixels centered at the origin, will be denoted by ROI, and the region of exposure, a disc of radius r_e pixels centered at the origin, will be denoted by ROE. Let the essential support of the discrete scaling and wavelet ramp filters, the sampled versions of the continuous functions (45) with sampling interval T_s, be $2r_m$ samples and the support of the wavelet reconstruction filters (34) be $2r_r$ samples. Therefore the radius of the region of exposure is $r_e = r_i + r_m + r_r$ pixels. The amount of exposure in our algorithm normalized to the full exposure is given by

$$\frac{r_r + r_m + r_i}{R}.$$

In the Delaney and Bresler's algorithm [9] the exposure is given by

$$2^{-L} + \sum_{q=1}^{L} 2^{-q+1}\left(\frac{r_r + r_m + r_i}{R}\right),$$

where L is the number of levels in the wavelet filter bank. Similar exposure is required in DeStefano and Olson's algorithm [8]. Fig. 5 shows the relative amount of exposure versus the size of the region of interest in a 256×256 image for $r_m = r_r = 6$. The exposure in Delaney and Bresler's algorithm is also plotted for comparison.

A. Error Analysis

It is mentioned in [14] that the error in the interior Radon transform is not negligible because the derivative Hilbert transform (the impulse response of the filter $|\omega|$) is not local in space. This means that in order to reconstruct even a small local region of interest we have to consider some data outside the region of interest to get negligible reconstruction error. We will find an upper bound for the reconstruction error, in terms of the amount of non-local data that we consider in the reconstruction. We will also compare the upper bound of the error in a locally reconstructed image using our algorithm to the upper bound of the error when we use the standard filtered

backprojection method with local data. For simplicity of notation, we assume the ROI and ROE are centered at the center of the image. Consider the filtered backprojection formula (4), while the ramp filter $|w|$ is replaced by a generally angle dependent filter $h_\theta(s)$

$$f_r(x,y) = \int_0^\pi (h_\theta(s) * R_\theta f(s))(x\cos\theta + y\sin\theta)d\theta. \tag{46}$$

If $h_\theta(s)$ is chosen to be the impulse response of the ramp filter (5), the reconstructed function $f_r(x,y)$ is an approximation of the function f; and if it is the impulse response of the wavelet and scaling ramp filters (45), the reconstructed function $f_r(x,y)$ will be the approximation of the wavelet and scaling coefficients. The discrete version of (46) is given by

$$f_r(x,y) = \frac{\pi}{K}\sum_{k=1}^{K}(\frac{1}{R}\sum_{n=-R}^{R} P_{\theta_k}(n)h_{\theta_k}(m-n)), \tag{47}$$

where $m = \lfloor \frac{x\cos\theta + y\sin\theta}{T_s} \rfloor \in ROE$, K is the total number of evenly spaced angles at which the projections are measured, $P_{\theta_k}(n)$ is the projection $R_{\theta_k}f(\frac{n}{T_s})$, and $\theta_k = k\frac{\pi}{K}$. We can divide the inner summation into two parts, corresponding to the ROE and its complement $\overline{ROE}$:

$$\begin{aligned} f_r(x,y) &= \frac{\pi}{K}\sum_{k=1}^{K}(\frac{1}{R}\sum_{|n|\le r_e} P_{\theta_k}(n)h_{\theta_k}(m-n)) \\ &+ \frac{\pi}{K}\sum_{k=1}^{K}(\frac{1}{R}\sum_{|n|> r_e} P_{\theta_k}(n)h_{\theta_k}(m-n)). \end{aligned} \tag{48}$$

Thus the magnitude of error using only ROE is given by

$$|e(x,y)| = |\frac{\pi}{K}\sum_{k=1}^{K}(\frac{1}{R}\sum_{|n|> r_e} P_{\theta_k}(n)h_{\theta_k}(m-n))|. \tag{49}$$

To get an upper bound for the error we use the Cauchy-Schwartz inequality as

$$\begin{aligned} |e(x,y)| &= |\frac{\pi}{K}\sum_{k=1}^{K}(\frac{1}{R}\sum_{|n|> r_e} P_{\theta_k}(n)h_{\theta_k}(m-n))| \\ &\le \frac{\pi}{K}\sum_{k=1}^{K}(\frac{1}{R}\sum_{|n|> r_e} |P_{\theta_k}(n)h_{\theta_k}(m-n)|) \\ &\le \frac{\pi}{K}\sum_{k=1}^{K}\frac{1}{R}\,(\sum_{|n|> r_e}|P_{\theta_k}(n)|^2)^{1/2}(\sum_{|n|> r_e}(|h_{\theta_k}(m-n)|^2)^{1/2}\,. \end{aligned} \tag{50}$$

If we assume that the support of $f(x,y)$ is in the disc of radius 1, then $|P_{\theta_k}(n)| \le 2\max|f(x,y)|$. Hence

$$|e(x,y)| \le \frac{4\pi}{K}\max|f(x,y)|\frac{R-r_e}{R}\sum_{k=1}^{K}(\sum_{|n|> r_e}|h_{\theta_k}(m-n)|^2)^{1/2}. \tag{51}$$

We define the relative error as $|e_{rel}(x,y)| = \frac{|e(x,y)|}{\max|f(x,y)|}$, then

$$|e_{rel}(x,y)| \leq \frac{4\pi}{K}\frac{R-r_e}{R}\sum_{k=1}^{K}(\sum_{|n|>r_e}|h_{\theta_k}(m-n)|^2)^{1/2}. \tag{52}$$

In the worst case the region of interest is a single point. Thus we may bound (52) by

$$|e_{rel}(x,y)| \leq \frac{4\pi}{K}\frac{R-r_e}{R}\sum_{k=1}^{K}(\sum_{|n|\geq r_e-r_i}|h_{\theta_k}(n)|^2)^{1/2}. \tag{53}$$

We define $h^T_{\theta_k}$, the truncated filter, as

$$h^T_{\theta_k}(n) = \begin{cases} h_{\theta_k}(n) & |n| < r_e - r_i \\ 0 & \text{otherwise} \end{cases}. \tag{54}$$

Therefore

$$|e_{rel}(x,y)| \leq \frac{4\pi}{K}\frac{R-r_e}{R}\sum_{k=1}^{K}(\sum_{n=-R}^{R}|h_{\theta_k}(n)-h^T_{\theta_k}(n)|^2)^{1/2}. \tag{55}$$

The inner sum can be written in frequency domain, thus

$$|e_{rel}(x,y)| \leq \frac{4\pi}{K}\frac{R-r_e}{R}\sum_{k=1}^{K}(\sum_{m=-R}^{R}|H_{\theta_k}(m)-H^T_{\theta_k}(m)|^2)^{1/2}, \tag{56}$$

where H_{θ_k} and $H^T_{\theta_k}$ are the Fourier transform of h_{θ_k} and $h^T_{\theta_k}$, respectively. The upper bound of the error in standard filtered backprojection method can be calculated by replacing $h_{\theta_k}(m)$ in (56) by the ramp filter (5). The upper bound for the error in wavelet and scaling reconstruction can be obtained by replacing H_{θ_k} in (56) with (45). In our algorithm, the scaling and wavelet coefficients at resolution 2^{-1} are reconstructed directly from the projection data. The recovered coefficients are then filtered by the reconstruction filters (34) to obtain the original image. These filters will filter out some parts of error energy introduced by (56). To consider the effect of the wavelet reconstruction filter bank in the error upper bound, we moved these filters to the projection domain, hence

$$\begin{aligned}|e_{rel}(x,y)| \leq \frac{4\pi}{K}\frac{R-r_e}{R}\sum_{k=1}^{K} & (\sum_{m=-R}^{R}|E^A_{\theta_k}(m)|^2)^{1/2}+(\sum_{m=-R}^{R}|E^{D^1}_{\theta_k}(m)|^2)^{1/2} \\ + & (\sum_{m=-R}^{R}|E^{D^2}_{\theta_k}(m)|^2)^{1/2}+(\sum_{m=-R}^{R}|E^{D^3}_{\theta_k}(m)|^2)^{1/2},\end{aligned} \tag{57}$$

where

$$
\begin{aligned}
E^{A}_{\theta_k}(m) &= (H^{A}_{\theta_k} - H^{A\,T}_{\theta_k}) H^{A}_{r}(m\cos\theta_k, m\sin\theta_k) \\
E^{D^1}_{\theta_k}(m) &= (H^{D^1}_{\theta_k} - H^{D^1\,T}_{\theta_k}) H^{D^1}_{r}(m\cos\theta_k, m\sin\theta_k) \\
E^{D^2}_{\theta_k}(m) &= (H^{D^2}_{\theta_k} - H^{D^2\,T}_{\theta_k}) H^{D^2}_{r}(m\cos\theta_k, m\sin\theta_k) \\
E^{D^3}_{\theta_k}(m) &= (H^{D^3}_{\theta_k} - H^{D^3\,T}_{\theta_k}) H^{D^3}_{r}(m\cos\theta_k, m\sin\theta_k),
\end{aligned} \tag{58}
$$

with $H^{A}_{\theta_k}$,$H^{D^1}_{\theta_k}$,$H^{D^2}_{\theta_k}$ and $H^{D^3}_{\theta_k}$ being the ramped scaling and wavelet filters (45) and $H^{A\,T}_{\theta_k}$,$H^{D^1\,T}_{\theta_k}$,$H^{D^2\,T}_{\theta_k}$ and $H^{D^3\,T}_{\theta_k}$ being the truncated version of these filters. H^{A}_{r}, $H^{D^1}_{r}$, $H^{D^2}_{r}$, and $H^{D^3}_{r}$ are the wavelet reconstruction filters (34). Fig. 6(a) compares the upper bound of the relative error in the reconstructed image, versus the amount of non-local data $(r_e - r_i)$. This bound is given by (56) and (57) for the standard filtered backprojection method and our algorithm, respectively. When we use the biorthogonal wavelet of Fig. 3, our algorithm has much less error, than the standard filtered backprojection method, but for the orthogonal basis of Fig. 4, the reconstruction error is larger (Fig. 6(b)). Therefore we choose the biorthogonal wavelet of Fig. 3 in our algorithm. The horizontal axis in Fig. 6(a) shows the amount of non-local data that is collected in order to reconstruct the region of interest. It shows that if we expose a margin of 6 pixels outside the region of interest, the upper bound for the relative error would be as small as .004. Therefore we can assume that the essential supports of the wavelet and scaling ramp filters are 6 pixels.

B. Interior Problem

The interior problem in even dimensions is not uniquely solvable, since there are non-zero functions which have zero projections on the ROE. Clearly, our algorithm will be unable to reconstruct such a function. It has been noted that these functions, which are in the null-space of the interior problem, do not vary much well inside the ROE [14]. Since in our algorithm the ROE is larger than the ROI by a fixed margin, it is observed that the null-space elements described above are essentially constant on the ROI.

To illustrate this, we will reconstruct an element of the null-space and measure the variance of this element on the ROI. We assume that the ROI is the interior 32 pixels of the image and ROE is the ROI plus a margin of 12 pixels in each side. This margin shows the amount of nonlocal data used in the reconstruction scheme. Fig. 7(b) shows a slice of a circularly symmetric element of the

null-space. The projection of this element for each angle is shown in Fig. 7(a) . The projections are zero inside the ROE, which is the interior 56 pixel of the projections, and one in 16 pixels at each side of the ROE. The measured variance of the null-space on the ROI is less than 1 percent. The variance of the null-space element on the ROI versus the amount of nonlocal data (the difference of the radius of the ROE and ROI) is shown in Fig. 8.

V. Implementation

A. Practical Considerations

In local reconstruction, artifacts are common close to the boundary of the region of exposure. To illustrate this, we consider the Shepp-Logan head phantom and an ROE of diameter 32 pixels at the center of the image. We set the projections outside the ROE to zero (Fig. 9(c)) and apply the filtering part of the filter backprojection formula (5). Fig. 9(d) shows the artifacts that appear at the borders of the region of exposure. When the standard filtered backprojection algorithm is applied to the projections, these artifacts cause large errors at the borders of the region of exposure in the reconstructed image.

In order to avoid the artifacts, we have extrapolated the projections continuously to be constant on the missing projections. The extrapolation scheme is the same even when the region of exposure is not centered. Let the region of exposure, which is the subset of projections on which $R_\theta f$ is given, be a circle of radius r_e whose center is located at polar coordinates (r, θ_0), i.e,

$$ROE: \ \{ \ s : s \in [\ r \ \cos(\theta - \theta_0) - r_e, \ r \ \cos(\theta - \theta_0) + r_e \ ] \ \}. \tag{59}$$

We use the constant extrapolation

$$(R_\theta)_{local}(s) = \begin{cases} R_\theta(s) & \text{if } s \in ROE \\ R_\theta(r \ \cos(\theta - \theta_0) + r_e) & \text{if } s \in [\ r \ \cos(\theta - \theta_0) + r_e, \ +\infty) \\ R_\theta(r \ \cos(\theta - \theta_0) - r_e) & \text{if } s \in (\ -\infty, \ r \ \cos(\theta - \theta_0) - r_e] \end{cases} . \tag{60}$$

Fig. 9(e) and 9(f) show an extrapolated projection and its ramp-filtered version (5), respectively. When we apply the ramp filter to the extrapolated projection, there is no spike at the edge of the region of exposure. The comparison with the ramp-filtered version of the projection using global data (Fig. 9(b)) shows that the filtered projection has a constant bias difference compared

to the one using global data. This is natural in local tomography and, after backprojection of all projections, appears as a constant bias in the locally reconstructed image ([14],[16]).

In [14] it is suggested to extrapolate the data outside the region of interest using a minimum norm approach which has the same effect on the artifacts (cf. Fig. VI.8 in [14]).

B. Algorithm

We have noted that the approximation can be reconstructed locally using local data. Therefore in our algorithm we reconstruct the wavelet and scaling coefficients at resolution 2^{-1} and then we reconstruct the image from these coefficients. Our algorithm consists of the following steps:

1. Extrapolate the locally collected projections using (60) to avoid the boundary artifacts.
2. Filter the extrapolated projections by modified ramp filters (45).
3. Backproject the filtered projections to every other point, using (39), to obtain the approximation (41) and detail (43) coefficients at resolution 2^{-1}.
4. Upsample the reconstructed coefficients by 2 and filter them by the reconstruction filters (33) to obtain the image at resolution 1.

VI. Simulation Results

We have obtained the wavelet and scaling coefficients of the 256×256 pixel image of the Shepp-Logan head phantom using global data (Fig. 11). In this decomposition we used the Daubechies' biorthogonal basis (table III of [5]). The quality of the reconstructed image is the same as with the filtered backprojection method (cf. Fig. 10). Fig. 12 and 13 show two examples in which two regions of interest are reconstructed using the local reconstruction method proposed in this paper. In Fig. 12, the ROI is a centered disk of radius 32 pixels. Fig. 12(c) and 12(d) show the blow up of the ROI using both local reconstruction and standard filtered backprojection using global data for comparison. We have also reconstructed the off-center disk of radius 32 pixels located 80 pixels from the center of the image. The reconstructed image and the blow up of the ROI are shown in Fig. 13. In both of these examples the projections are collected from a disk of radius 44 pixels, therefore the amount of exposure is 17% of the conventional filtered backprojection method. In both cases we have a constant bias in the reconstructed image which is natural in the interior reconstruction problem [14] [16]. In these examples the mean square error between the original image and the

locally reconstructed image after removing bias is computed over the region of interest. [2] The error energy in the reconstructed image in both cases is the same as filtered backprojection method using full exposure data.

This method is applied to a CT scan image of a liver. The reconstructed image has the same quality as the filtered backprojection method (Fig. 14). Using our algorithm, a local off-centered region of radius 32 pixels of the liver CT scan has been reconstructed by using just 17% of exposure (Fig. 15). The reconstruction in the region of interest is as good as what can be obtained using the filtered backprojection method which involves global data and 100% exposure.

VII. Conclusion

We have developed an algorithm to reconstruct the wavelet and scaling coefficients of a function from its Radon transform. Based on the observation that for some wavelet bases with sufficiently many zero moments, the scaling and wavelet functions have essentially the same support after ramp filtering, we have developed a local reconstruction scheme to reconstruct a local region of a cross section of a body with essentially local data. An upper bound for the local reconstruction error is obtained in terms of the amount of non-local data which is used in the reconstruction scheme. Non-uniqueness of the interior problem appears as a constant bias in the reconstructed image. The measured error between the original image and the reconstructed image after removing this bias is negligible. This fact shows that if we use a sufficient amount of non-local data in the reconstruction, this bias is reasonably constant on the region of interest.

References

[1] D. Walnut, " Application of Gabor and wavelet expansions to the Radon transform," in *Probabilistic and Stochastic Methods in Analysis, with Applications*, J. Byrnes, et al. eds., Kluwer Academic Publishers, Inc., 187-205, 1992.

[2] C. Berenstein and D. Walnut, "Local inversion of the Radon transform in even dimensions using wavelets," in *75 Years of Radon Transform*, S. Gindikin, and P. Michor, eds., International Press Co., Ltd., 38–58, 1994.

[2]The mean square error is calculated using this equation

$$\frac{1}{N} \sum_{(n,m):(n,m)\in ROI} (f(n,m) - \hat{f}(n,m))^2,$$

where f is the original image, $\hat{f}$ is the reconstructed image with the constant bias removed, and N is the number of pixels in the ROI.

[3] A. Faridani, E. Ritman and K.T. Smith, "Local tomography", *SIAM J. Appl. Math.*, vol 52, no.2, pp. 459-484, Apr. 1992.

[4] A. Faridani, F. Keinert, F. Natterer, E. L. Ritman and K.T. Smith, "Local and global tomography", in *Signal Processing*, IMA Vol. Math., Appl., vol 23. New York: Springer-Verlag, New York, pp. 241-255, 1990.

[5] M. Antonini, M. Barlaud, P. Mathieu and I. Daubechies, "Image coding using wavelet transform," *IEEE Trans. Image Proc.*, vol. 1, no. 2, pp. 205-220, Apr. 1992.

[6] I. Daubechies, *Ten lectures on wavelets.* SIAM-CBMS series, SIAM, Philadelphia, 1992.

[7] S. Mallat, "A theory for multiresolution signal decomposition: The wavelet representation," *IEEE Trans. on PAMI*, vol. 11, no. 7, July 1989.

[8] J. DeStefano and T. Olson, "Wavelet localization of the Radon transform in even dimensions," *IEEE Trans. Signal Proc.*, vol. 42, no.8, Aug. 1994.

[9] A. H. Delaney and Y. Bresler, "Multiresolution tomographic reconstruction using wavelets," *IEEE Intern. Conf. Image Proc.*, vol. ICIP-94, pp. 830-834, Nov. 1994.

[10] K. T. Smith and F. Keinert, "Mathematical foundation of computed tomography," *Applied Optics*, vol. 24, No. 23, December 1985.

[11] Y. Zhang, M. Coplan, J. Moore, and C. A. Berenstein, "Computerized tomographic imaging for space plasma physics," *J. Appl. Physics*, vol. 68, 1990.

[12] G. Beylkin, R. Coifman, and V. Rokhlin, "Fast wavelet transforms and numerical algorithms," *Comm. Pure Appl. Math.*, vol. 44, 141–183, 1991.

[13] J. Guedon and M. Unser, "Least square and spline filtered backprojection," *preprint*, March 1994.

[14] F. Natterer, *The Mathematics of Computerized Tomography*, New York, Wiley, 1986.

[15] P. Maass, "The interior Radon transform," *SIAM J. Appl. Math*, vol. 52, No. 3, pp. 710-724, June 1992.

[16] A. K. Louis and A. Rieder, "Incomplete data problem in x-ray computerized tomography," *Numeriche Mathematik*, vol. 56, 1989.

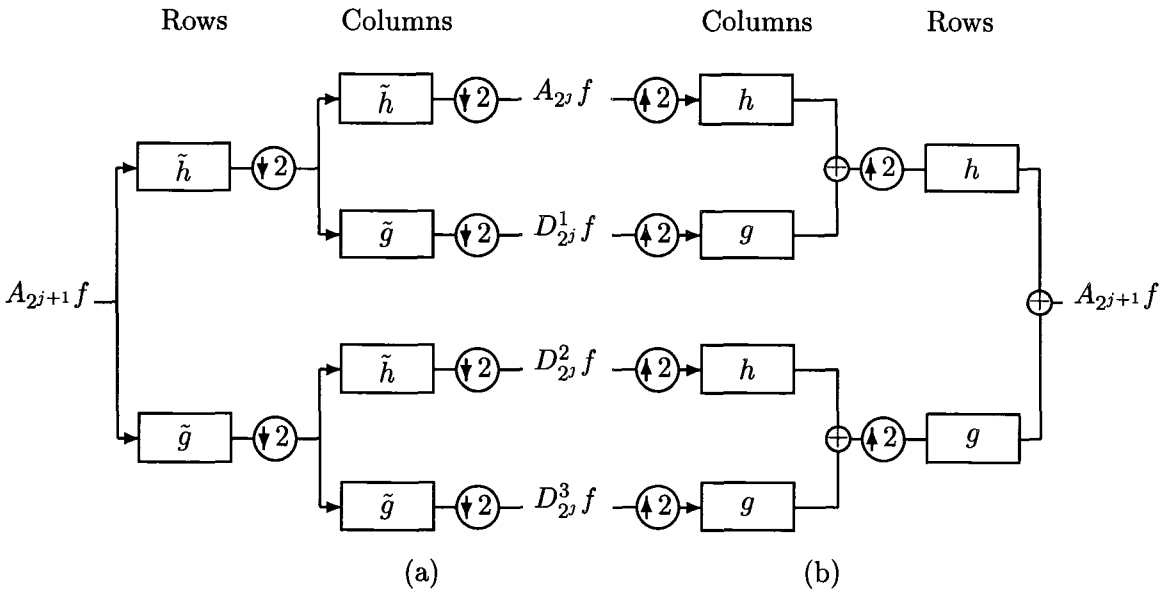

Fig. 1. (a) Wavelet synthesis filter bank; (b) wavelet analysis filter bank.

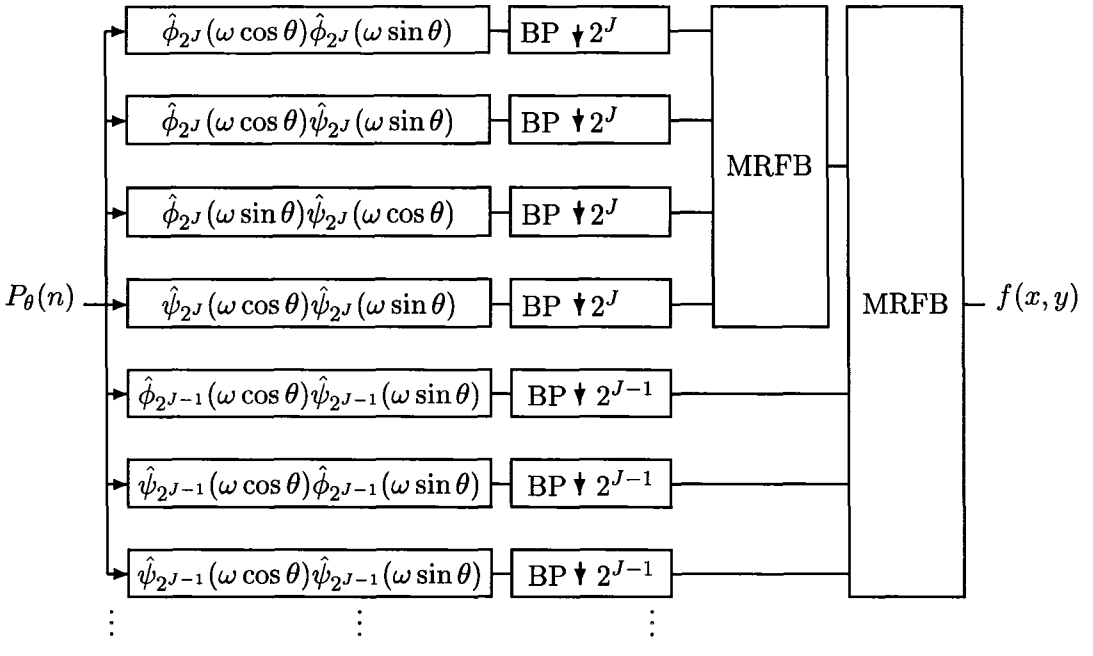

Fig. 2: Wavelet reconstruction from the projection data; the multiresolution reconstruction filter bank (MRFB) is the wavelet synthesis filter bank (Fig. 1).

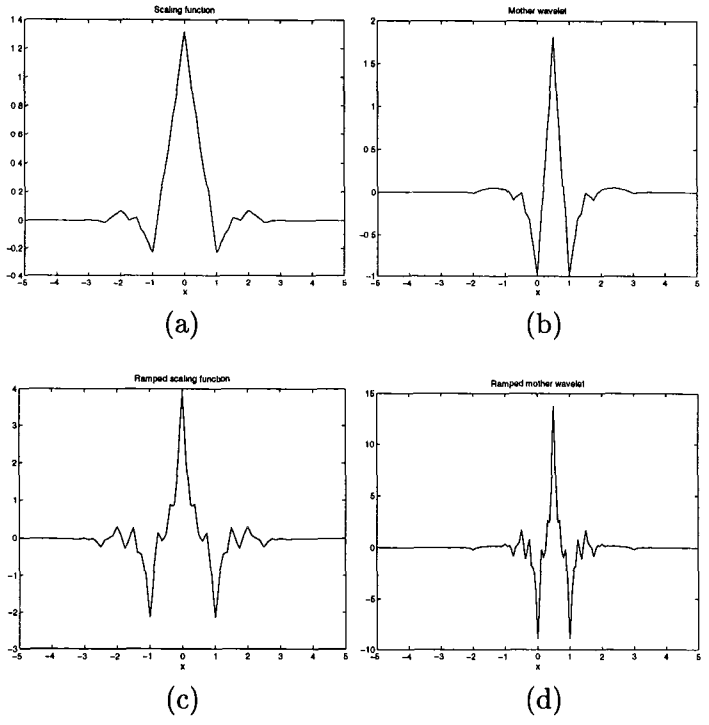

Fig. 3. The wavelet with less dissimilar lengths, $l = k = \tilde{k} = 4$; (a) the scaling function; (b) the wavelet basis; (c) the ramp–filtered version of the scaling function; (d) the ramp–filtered version of the wavelet basis.

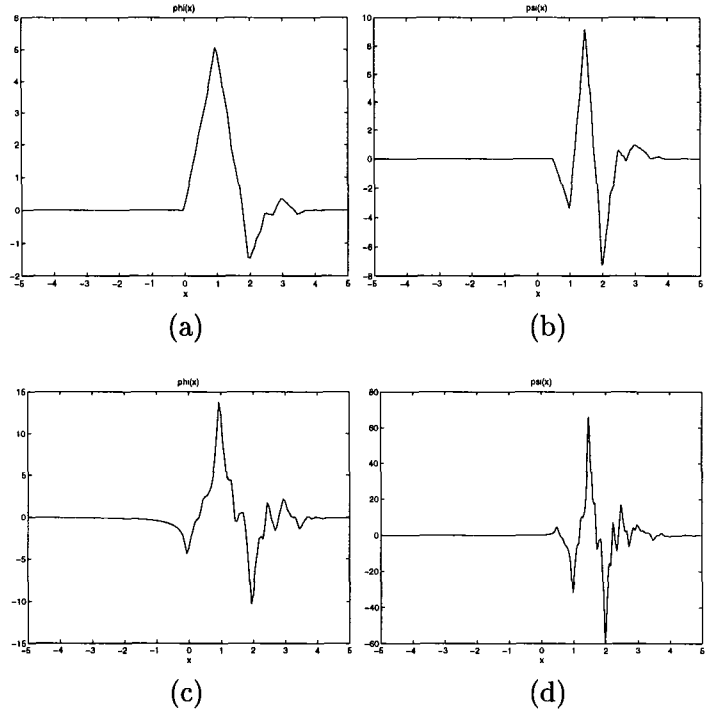

Fig. 4. The wavelet with extremal phase and highest number of vanishing moments with length 4; (a) the scaling function; (b) the wavelet basis; (c) the ramp–filtered version of the scaling function; (d) the ramp–filtered version of the wavelet basis.

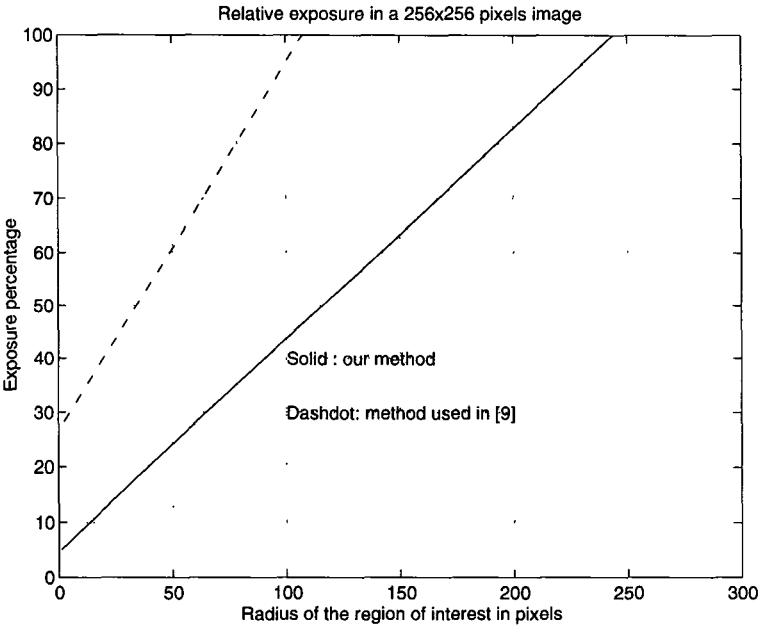

Fig. 5. The exposure percentage versus the size of the region of interest.

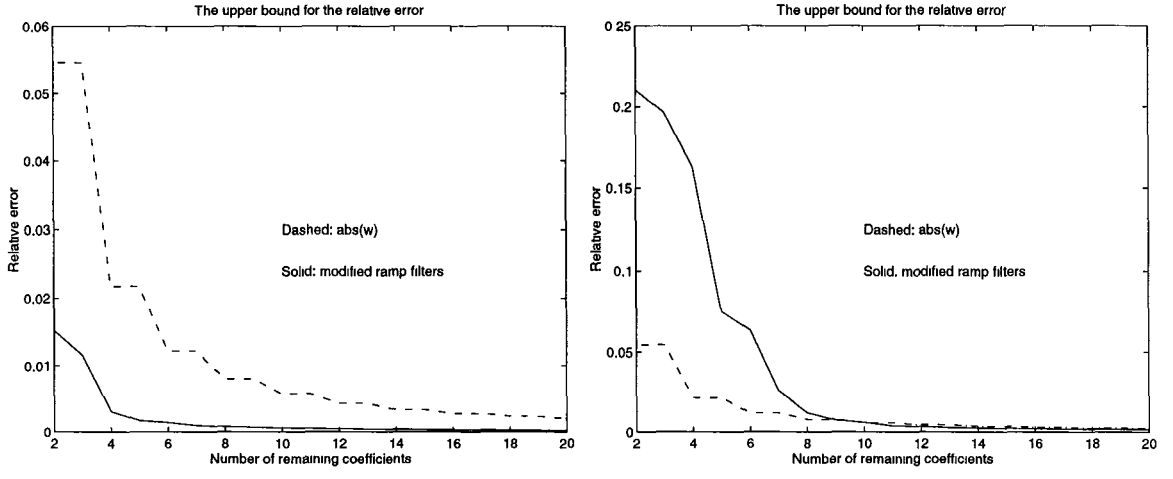

(a) (b)

Fig. 6: The error (57) versus the number of remaining coefficients; (a) in the biorthogonal wavelet with less dissimilar lengths (table III of [5]); (b) in the orthogonal wavelet with extremal phase and highest number of vanishing moments with length 4 (table 6.2 of [6]).

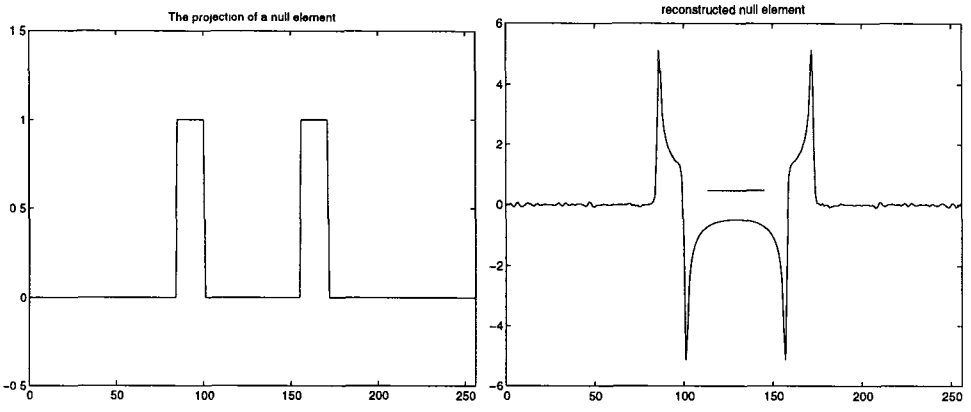

Fig. 7. (a) The projection of a null–space element; (b) the reconstruction of the null–space element. (The marked area is the region of exposure.)

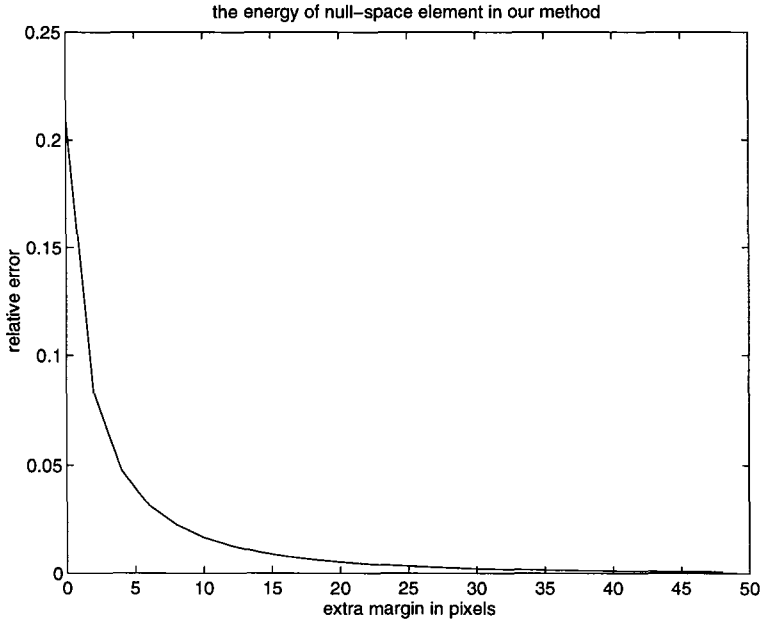

Fig. 8. The error versus the amount of non–local data used in the reconstruction scheme.

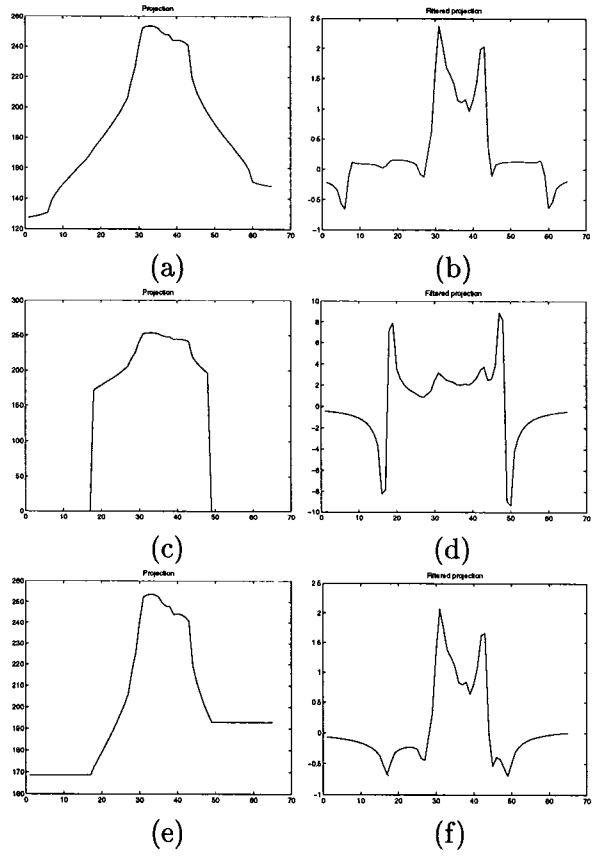

Fig. 9. (a) A sample projection of the Shepp-Logan head phantom; (b) the projection filtered by $|\omega|$; (c) the projection with non-local data set to zero; (d) the filtered projection; (e) the projection extrapolated outside the region of interest; (f) the ramp–filtered extended projection. (The marked area is the region of exposure.)

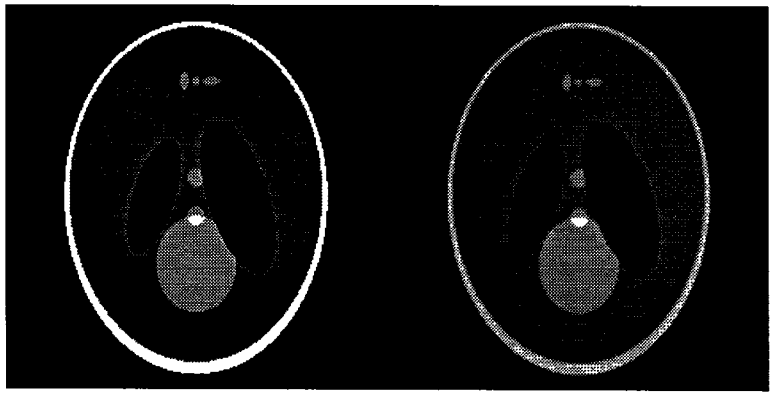

Fig. 10. (a) The Shepp-Logan head phantom; (b) the reconstruction using conventional filtered backprojection method.

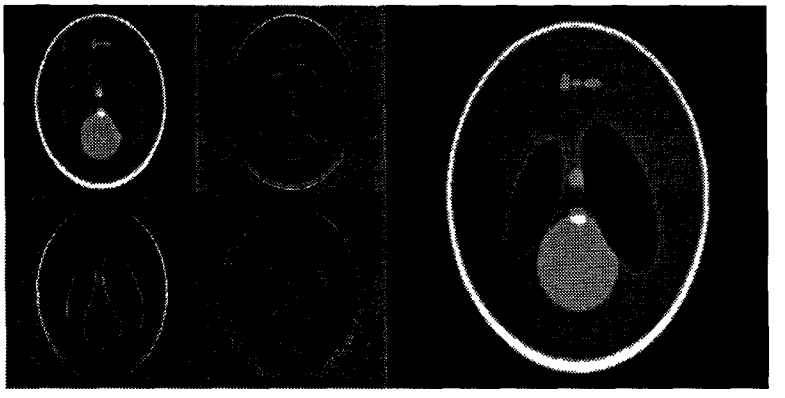

(a) (b)

Fig. 11. (a) Wavelet reconstruction; (b) the reconstruction from the wavelet coefficients.

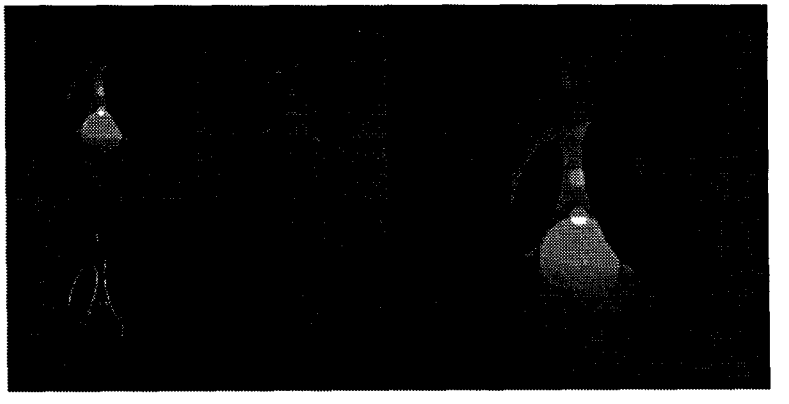

(a) (b)

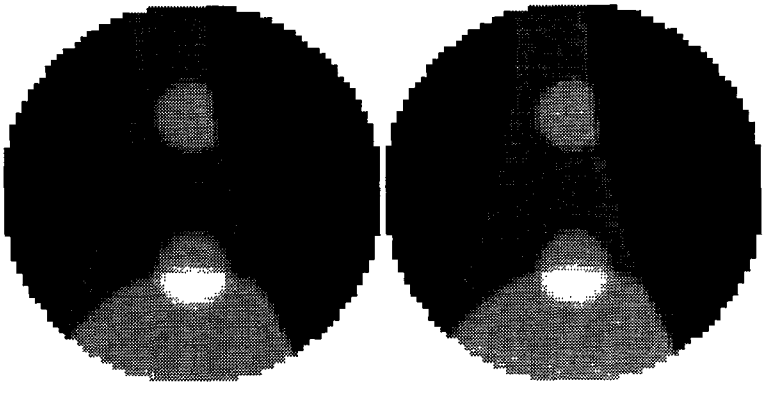

(c) (d)

Fig. 12. Local centered wavelet reconstruction; (a) wavelet reconstruction; (b) the reconstruction from the wavelet coefficients; blowup of the centered region of interest; (c) reconstruction using wavelet method using local data; (d) reconstruction using standard filtered backprojection method using global data.

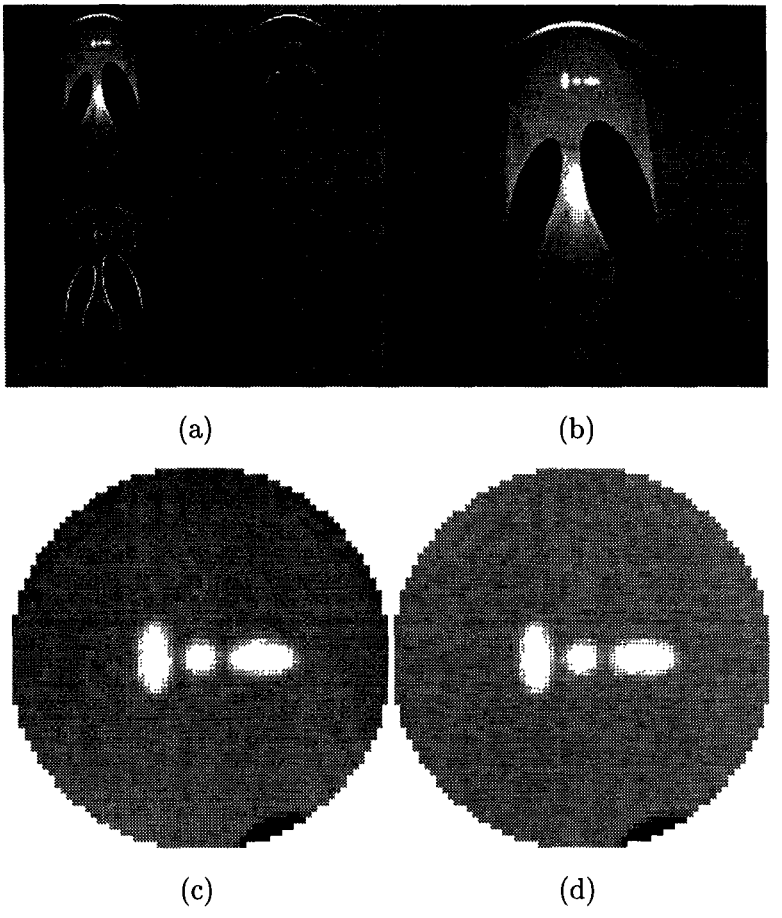

Fig. 13. Local off center wavelet reconstruction; (a) wavelet reconstruction; (b) the reconstruction from the wavelet coefficients; blowup of the off-center region of interest; (c) reconstruction using wavelet method using local data; (d) reconstruction using standard filtered backprojection method using global data.

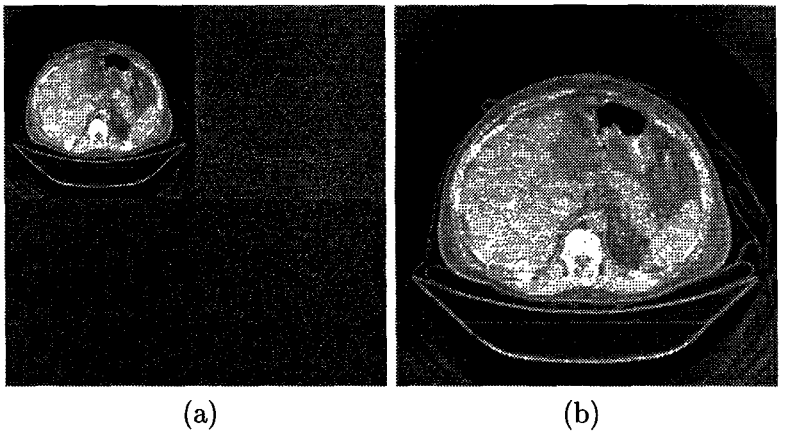

Fig. 14. (a) Wavelet coefficients using wavelet-Radon reconstruction; (b) the reconstructed image.

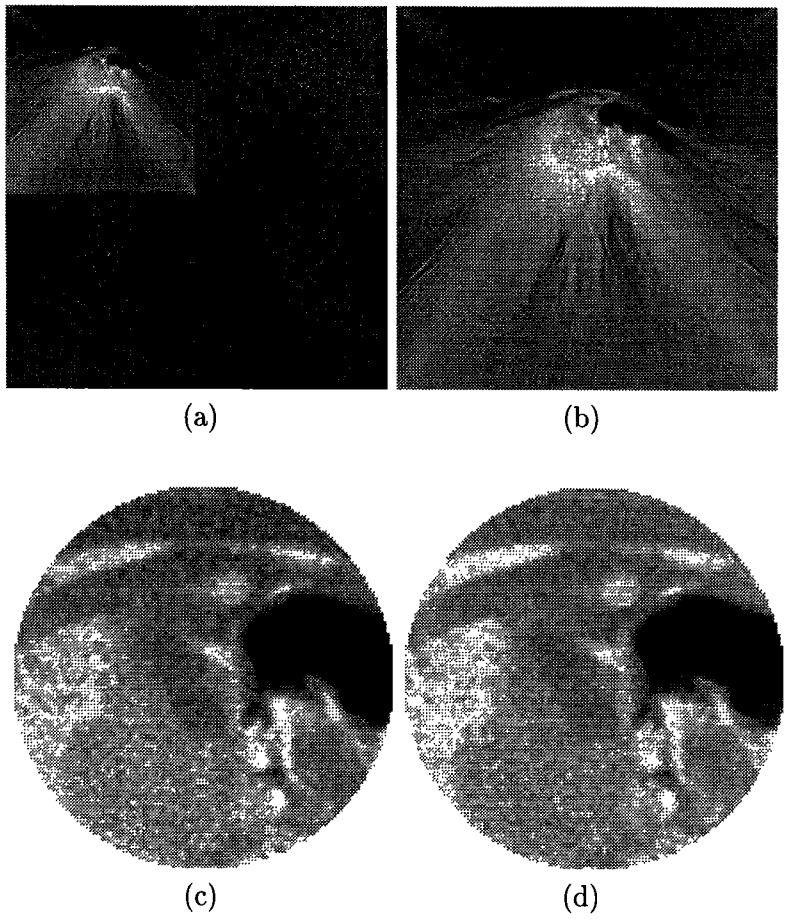

Fig. 15. Local off center wavelet reconstruction; (a) wavelet reconstruction; (b) the reconstruction from the wavelet coefficients; blowup of the off-center region of interest; (c) reconstruction using wavelet method using local data; (d) reconstruction using standard filtered backprojection method using global data.